



Cite this: DOI: 10.1039/d6an00004e

Stable focusing of proteins within a packed microbead bed by ion concentration polarization in a paper-based analytical device

Sommer Osman, Kira L. Rahn, Quinlan G. Pollak, Md Ruhul Amin and Robbyn K. Anand *

Paper-based analytical devices (PADs), and particularly lateral flow assays (LFAs), provide many advantages for protein sensing in clinical and resource-limited settings. This class of devices is an important tool for point-of-care (POC) diagnostics, but is limited by sensitivity, which is often inferior to standard benchtop instrumentation. Improvements in sensitivity would increase the range of accessible analytes for biological assays at the POC. Electrokinetic enrichment methods, such as ion concentration polarization focusing (ICPF), have been implemented for target analyte preconcentration. While ICPF has been demonstrated to achieve high enrichment factors (EFs) of proteins in PADs, the focused protein plug experiences instability, leading to bursting (downstream washout) or propagation (gradual upstream displacement) if convective forces are too strong or too weak. Here, we address these challenges by applying a patterned microbead bed to an ICP-PAD. The incorporation of the microbead bed is shown to fix the location of the dye-linked protein enrichment. In contrast, the ICP-PAD without beads exhibits bursting of the focused plug. Besides counteracting bursting, the microbead bed (μb) ICP-PAD increased the average EF by 5-fold and the maximum EF by 4-fold, with a peak EF of over 23-fold. Studies characterizing the effect of bead size were conducted and evaluated using parameters such as EF and the retained fraction of the plug to determine the bead diameters that prevent bursting. To evaluate the stability of the bed, we examined the fluorescence produced by a bed of stained microbeads before and after ICPF, and found less than 1% of fluorescence intensity lost. Finally, we leveraged the microbead bed as a test line for a biotinylated protein in a model LFA. We anticipate that this device architecture is broadly applicable to other real-world systems at the POC. These results establish a platform for the future integration of ICPF with LFAs for stable preconcentration and improved sensitivity of previously inaccessible protein targets.

Received 3rd January 2026,
Accepted 21st March 2026

DOI: 10.1039/d6an00004e

rsc.li/analyst

1. Introduction

Paper-based analytical devices (PADs) represent a class of critical technologies for biological sensing.¹ Paper offers many advantages as a support medium because it is inexpensive, abundant, portable, easily modifiable, and drives flow without an external pump.^{2–5} Numerous geometries and fabrication methods have been explored in PADs, with common detection schemes such as colorimetric, electrochemical, and luminescence.^{5–7} One of the most recognizable PADs includes lateral flow assays (LFAs) which are widely available for commercial use, a prominent example being the at-home pregnancy test.⁸ LFAs focus on protein detection and have been configured for a wide range of biomarkers.^{2,8} However, paper devices, and specifically LFAs, are limited by poor sensitivity

when compared to conventional techniques, hindering the range of applications that these platforms can be used at the point-of-care (POC).⁶ Improvements in sensitivity would aid in the sensing of previously inaccessible analytes in PADs for clinical and resource-limited settings.

Electrokinetics is one solution researchers have used for enhancing sensitivity and the limit of detection (LOD). Electrokinetic focusing leverages an applied electric field for the preconcentration of charged analytes.⁹ Several electrokinetic techniques have been integrated with PADs, such as ion concentration polarization (ICP), isotachopheresis (ITP), field-amplified sample stacking (FASS), and isoelectric focusing (IEF).^{9,10} ICP is an attractive candidate for preconcentration of real-life samples because it does not rely on specialized buffers and can sustain high enrichment factors (EF) for extended periods of time.¹¹ Additionally, ICP can be tuned to focus analytes in a specific location, such as over a test line in an LFA, increasing local analyte concentration at the capture zone and improving assay sensitivity.^{12–16}

The Department of Chemistry, Iowa State University, 2415 Osborn Drive, 1605 Gilman Hall, Ames, Iowa 50011-1021, USA. E-mail: rkanand@iastate.edu



ICP occurs when a voltage bias is applied on opposite sides of an ion-selective membrane or bipolar electrode.^{11,17} Ions are simultaneously enriched and depleted at opposing ends of the membrane or electrode, resulting in the formation of an ion enrichment zone (IEZ) and an ion depletion zone (IDZ). The IDZ is of particular interest because of its low conductivity and thereby, high electrical resistivity. At the IDZ boundary, a steep electric field gradient develops where charged analytes can be focused at the position in which convective and electromigratory forces are balanced.¹⁷ ICP of negatively charged analytes has been achieved on PADs by using a cation exchange membrane such as Nafion, as a resin^{18–25} or sheet.^{26–28} Several distinctive designs have also been developed, such as 3D folding structures^{29–31} and multilayer fabrication.^{12,32,33}

Gong *et al.* were the first to demonstrate active transport and preconcentration by ICP in a fully wet PAD, where manipulation of analytes post-wetting is generally not possible.²² To construct their PAD, they patterned Nafion, which served two functions: (1) defining fluidic regimes within the device and (2) providing the ion-selective structure necessary to induce ICP. As a proof-of-concept for protein applications, dye-linked albumin was enriched and the LOD was improved by 5-fold. Yang *et al.* confirmed ICP in PADs by measuring current-voltage curves (CVCs) of Nafion impregnated cellulose.²³ With centrifuge cap reservoirs and magnetic holders, they attained an enrichment factor (EF) of 15× for proteins. They improved upon their design by employing double-sided wax printing, which provided many advantages such as dampening electroosmotic flow (EOF).²⁰ High enrichment factors of protein were described. In all these cases, the device designs are not conducive to integration with existing assays, because Nafion is applied directly on the lateral flow paper, which disturbs fluid flow through the PAD. To combat this challenge, Han *et al.* devised a three-layer device where Nafion was patterned directly on tape, and then sandwiched both sides of the paper channel. This sealing effect had the added benefit of preventing evaporation by Joule heating, while also increasing contact between the channel and membranes.³² In this scheme, protein was enriched by more than 300-fold. Despite sufficient enrichment, these studies used wax printing as part of the fabrication process for their respective PADs. Solid ink wax printers are no longer commercially available, having been discontinued in 2016.^{34,35} In light of this, researchers are moving away from utilizing wax and investigating other materials for the manufacturing of PADs. Additionally, a major challenge in ICP-PADs is the instability of the focused plug. During ICP, if convective forces are too weak, the analyte will propagate upstream as the IDZ continues to grow. On the other hand, if convective forces are too strong, the IDZ is overtaken and unable to maintain the necessary balance of forces for focusing and consequently, the analytical plug bursts downstream.^{36,37} While Han *et al.* achieved high EFs, the focused protein's location was seen to propagate along the channel from $t = 100$ s to $t = 600$ s.³² To mitigate this effect, Yang *et al.* proposed a voltage control strategy, where the

voltage is stepped from a higher initial voltage to a lower voltage for the remainder of the experiment, permitting the sample plug maximum EF to be held for only 10 s.²³ In their double-sided wax printed PAD, they noted the anionic analyte dispersed completely during ion concentration polarization focusing (ICPF).²⁰ To avoid this effect, they preconcentrated the fluorescent tracer on the cathodic side of their device so that it accumulated in the IEZ, with Nafion serving as a barrier to further motion.

To address the nonlinear effects in the IDZ during ICPF, our lab established a platform for stable preconcentration of analytes in a microfluidic device. Berzina *et al.* leveraged packed microbeads to serve as geometric restrictions for confining vortices produced by the IDZ.³⁸ They observed the rate of enrichment of a fluorescent tracer was greater in the presence of packed microbead beds and most importantly, uniformly distributed along the channel width in a confined location. Recently, our lab has developed a paper-based ICP preconcentrator that was integrated with an LFA. Rahn *et al.* evaded modifying the lateral flow paper by sandwiching Nafion-coated electrodes in a multi-layer device. After several optimizations, SARS-CoV-2 spike protein was enriched in low conductivity running buffer over a test line to enhance the signal by nearly 3-fold.¹² These two approaches are not mutually exclusive; in fact, we find that applying patterned microbeads in the paper fluidic platform leads to a synergistic effect, which is presented herein.

In this paper, we perform electrokinetic enrichment of a dye-lined protein in dilute sample solutions using a microbead bed for stabilization of the focused plug. We have combined the previously mentioned studies from our lab to achieve protein enrichment in a fixed location during paper-based ICPF. The key finding is that the incorporation of microbeads in paper suppresses bursting of the enriched protein plug during the enrichment process. However, PADs that contained no beads displayed analyte bursting during ICPF. Moreover, the ICP-PAD with a packed microbead bed improved the average EF by 5-fold and the maximum EF by 4-fold, in comparison to the no beads case, achieving a peak EF of over 23-fold. We characterized the effect of bead size and found that while 0.2- and 0.5 μm beads had comparable performance, 1.0 μm beads displayed significant bursting after initial, rapid enrichment. Additionally, we observe increasing retention of the protein plug over time for the cases of 0.2 μm and 0.5 μm beads, and a sharp decrease in retention for 1.0 μm and no beads. The reported system provides significant advantages over existing PADs such as the following: (1) a simple, wax-free fabrication method that employs off-the-shelf microbeads customizable for users' needs, (2) a greater fraction of analyte available for potential downstream analyses, and (3) the ability to maintain the plug position during preconcentration, which is critical for kinetically slow interactions. Finally, we demonstrate that the microbead bed is stationary under the performed experimental conditions and that it can be used as a test line for capturing analytes of interest in an LFA. These results provide the foundation for future studies that incorpor-



ate the ICP-PAD with a packed microbead bed together with established LFAs for improved sensitivity.

2. Experimental section

2.1. Chemicals and materials

Albumin from Bovine Serum (BSA) with Texas Red Conjugate was obtained from Invitrogen (Carlsbad, CA). Pluronic F-127 and Nafion perfluorinated resin solution were ordered from Sigma Aldrich (St Louis, MO). Tween-20 and Tris-HCl (1.0 M solution) were purchased from Fisher Scientific (Waltham, MA). All solutions were prepared using double deionized water (18.2 M Ω cm) purified by a Sartorius Arium Pro UV Ultrapure Water System (Göttingen, Germany). Biotin Conjugation Kit (Fast, Type B), Lightning Link[®] was purchased from Abcam (Eugene, OR). Sodium Azide, 5% (w/v) and Tris-HCl (1.0 M solution) were purchased from Fisher Scientific (Waltham, MA). Slide-A-Lyzer Dialysis Cassettes (10 K MWCO) were obtained from Thermo Scientific (Waltham, MA).

For electrode and device fabrication, the following were purchased: nitrocellulose membranes, 0.45 μ m pore size, from Thermo Scientific (Waltham, MA), SuperAvidin[™] Coated Microspheres ($d = 0.2, 0.5, \text{ and } 1.0 \mu\text{m}$) and SuperAvidin[™] Coated/Dragon Green Microspheres ($d = 0.2 \mu\text{m}$) from Bangs Laboratories (Fishers, IN), cellulose fiber sample pads from Millipore Sigma (Burlington, MA), backing cards from DCNovations (Carlsbad, CA), microfluidic diagnostic tape from 3 M (9964, St Paul, MN), Ag/AgCl ink from Nagase ChemTeX American Corporation (CI-4002, Delaware, OH), and Whatman filter paper Grade 1, from Fisher Scientific (Waltham, MA).

2.2. Device design and fabrication

Sample and adsorbent pads. The cellulose fiber sample pads (Fig. 1A and C) were cut into 2.0 \times 2.0 cm squares, then pretreated with blocking buffer (Pluronic F-127) and dried overnight. The absorbent pads (Fig. 1A and C) consisted of Whatman filter paper cut into the shape of a Pac-Man (a circle with a 90° sector removed) to maintain a steady capillary flow rate.^{12,39}

Nafion-coated electrodes stenciling on the backing cards. Electrodes were first designed on CorelDraw (Coral Co., Canada) to the following dimensions: 5.0 mm \times 10.0 mm and spaced 5.0 mm apart. Using a 75 W Epilog Fusion M2 CO₂ laser (Epilog Laser, Golden, CO), the electrode design was stenciled onto transparency films. The electrodes were fabricated by applying a thin layer of Ag/AgCl ink onto each stencil, overlaying a clean transparency film. The stencil was then removed to reveal driving electrodes, which were then left to dry at ambient temperature overnight. The stencil was wiped clean and stored for future use. Photographs of the stencil-printed Ag/AgCl electrodes are shown in Fig. 1B. One flexible transparency sheet can house 25 pairs of driving electrodes at once, before being cut to size. Electrodes were directly patterned with Nafion to induce the ICP process. This Nafion patterning process has been previously described in detail.¹² Briefly, Ag/

AgCl electrodes were cut to size and affixed to either (a) adhesive backing cards to form the bottom layer of the device or (b) diagnostic tape to form the top layer. An Automated Lateral Flow Reagent Dispenser (ALFRD) purchased from Claremont Bio (Upland, CA) was used to dispense Nafion onto the left and right-hand electrodes at a flow rate of 8.0 $\mu\text{L s}^{-1}$ with a dispenser voltage of 3.0 V. Finally, the Nafion-coated electrodes were baked at 65.0 $^{\circ}\text{C}$ for 10 min and then soaked in deionized water overnight before further use. After a period of three days, unused electrodes were disposed of safely.

Microbead preparation and bed packing. To construct the microbead bed, an aliquot of bioconjugated (superavidin-coated) microspheres was mixed with wash buffer (0.05% Tween-20 in deionized water) at a 1 : 10 ratio. The bead suspension was centrifuged at 11 600 rpm for 5 min. The supernatant was discarded, and the beads were resuspended to a concentration of 15.0 mg mL⁻¹. To pack the microbead bed, a flat-tipped micropipette dispensed 4.0 μL of the bead suspension across the entire width of the nitrocellulose at a distance of 14.0 mm from the left-hand edge (the end employed for sample introduction). The nitrocellulose membranes had been previously cut to the dimensions of 0.5 mm \times 25.0 mm by a guillotine cutter. After packing, the nitrocellulose strips were left to dry for 30 min at room temperature and then blocked with 1.0 mM Pluronic F-127. Blocking was achieved by allowing the nitrocellulose strips to wick the blocking solution through their entire length before being hung to dry for 30 min. Any prepared nitrocellulose strips were utilized immediately and always prepared on the same day of the experiments.

Device assembly. To assemble the devices, the Nafion-coated electrodes imprinted on the backing cards were affixed to a glass slide to form the bottom layer. The nitrocellulose strip was then aligned by hand so that the microbead bed bordered the right-hand Nafion membrane and there was a 5.0 mm gap between the edge of the strip and the Ag/AgCl driving electrodes (Fig. 1A). The top layer, consisting of Nafion-coated electrodes patterned on diagnostic tape, was then aligned to exactly overlay the electrodes in the bottom layer. The diagnostic tape helped to seal the device between the four Nafion membranes and prevent evaporation by Joule heating. Finally, the sample and absorbent pads were fastened to the backing card at a distance of 5.0 mm away from each Nafion membrane.

2.3. Experimental procedure

300 μL of sample solution (80 nM Biotinylated Texas Red BSA in 100.0 mM Tris, 0.05% Tween-20, pH 8.2) was applied to the sample pad and allowed to wick for 15 min, so that the solution reached the absorbent pad for a constant flow rate. Voltage was applied across the device for a period of 20 min using a Tektronix 2260B DC power supply (Tektronix, Beaverton, OR). The 20 min enrichment time was selected based on prior studies of ICP-enhanced LFAs showing that fluorescence intensity approaches a plateau after approximately 20 min of enrichment.¹² We therefore used 20 min to



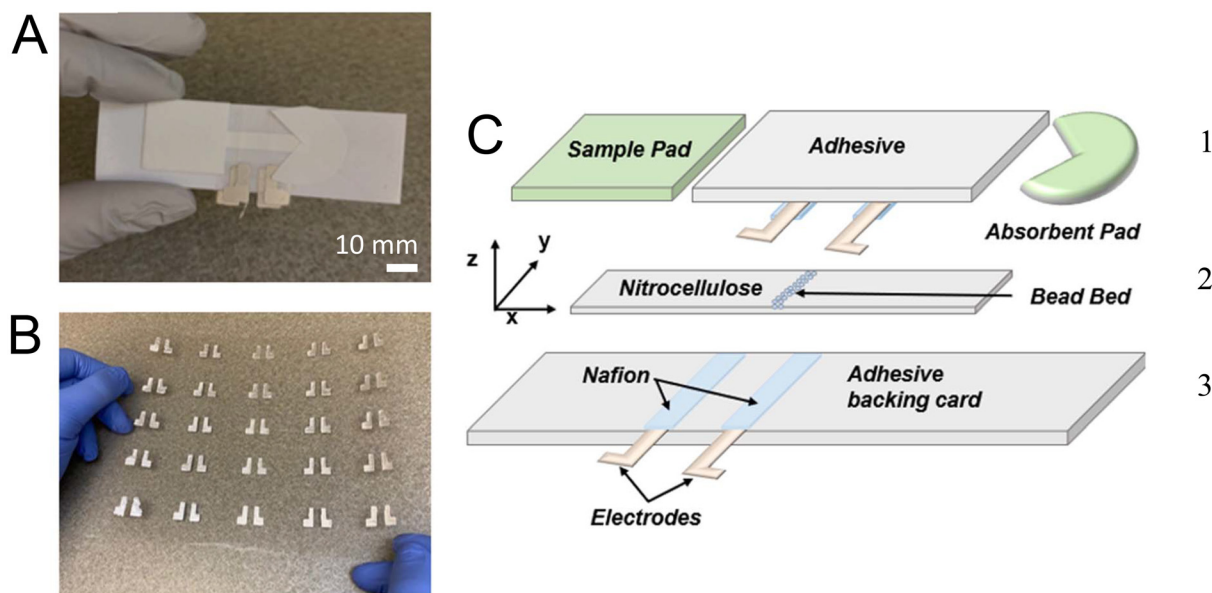


Fig. 1 The paper-based ICP device and its components. (A) Photograph of the assembled device and its associated layers. (B) Photograph of the stencil-printed Ag/AgCl electrodes on transparency sheets. (C) A side-view schematic of the ICP-enhanced LFA. Layer 1 (from left to right): cellulose sample pad, two cation-selective Nafion membranes (light blue) mounted on a microfluidic diagnostic tape and attached to two AgCl ink electrodes (tan), and a Pac-Man-shaped filter paper waste pad. Layer 2: a nitrocellulose membrane with a bead bed (test line) (light blue circles). Layer 3: two Nafion cation-selective membranes (light blue) coated on an adhesive backing card (light grey) that connects to two AgCl ink electrodes (tan).

ensure sufficient enrichment while maintaining consistent comparison between device architectures.

2.4. Imaging and analysis

All images were obtained on an SMZ800N stereoscope (Nikon Industries, New York, NY) equipped with a Sola Lumencor Light engine (Lumencor, Beaverton, OR) and Photometrics Cool Snap Dyno camera (Tucson, AZ). Fluorescence micrographs were obtained every 20 s for a period of 35 min to monitor the local concentration and position of Texas Red BSA between the Nafion membranes. Fluorescence image analysis was performed using a custom script in MatLab (MathWorks, Natick, MA). To confirm the amount of fluorescence produced by the microbead bed before and after the ICP process, ImageJ (National Institute of Health, Bethesda, MD) was used. All fluorescence micrographs were background-subtracted.

Scanning electron microscopy (SEM) micrographs were obtained using a FEI Quanta-FEG 250™ SEM instrument (Hillsboro, OR) with an accelerating voltage of 10 kV. The samples were coated with approximately 5 nm of iridium to provide conductivity necessary for SEM imaging.

3. Results and discussion

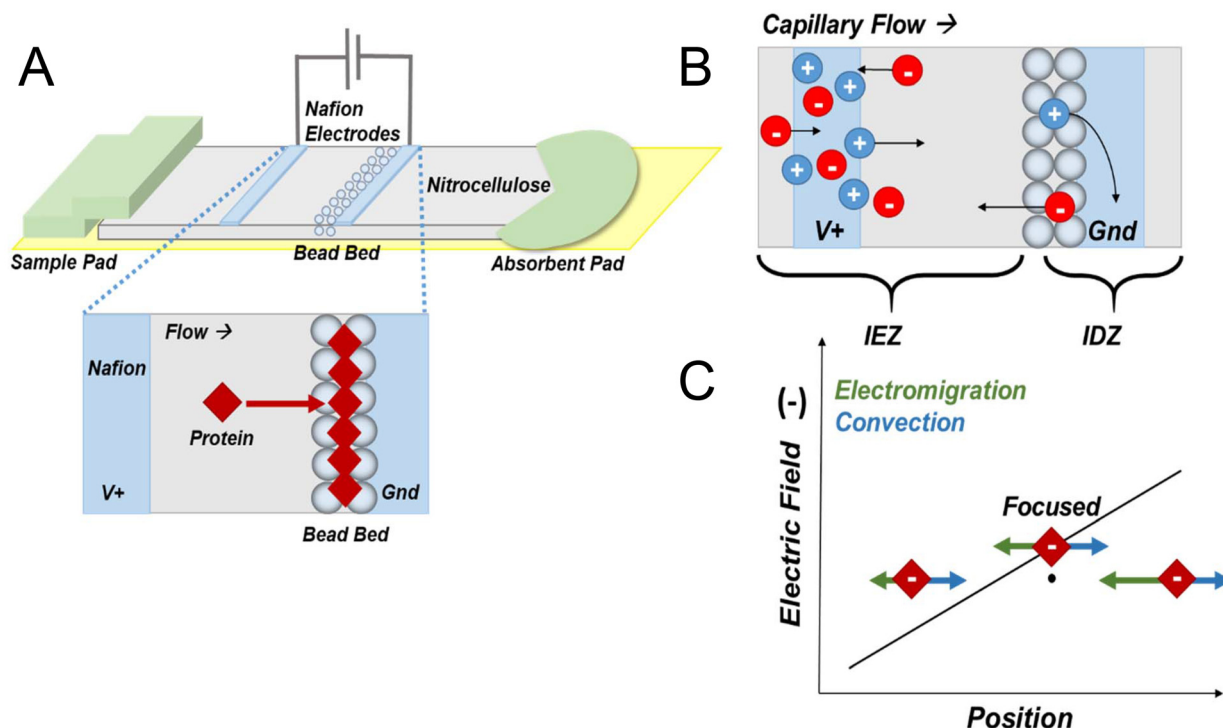
3.1. Incorporation of a microbead bed in the ICP-PAD

Scheme 1A shows the components of the ICP-PAD with a patterned microbead bed (μ b-ICP-PAD). The sample pad and Pac-Man-shaped absorbent pad (Scheme 1A) overlay the paper channel, and the entire device is supported by a backing card

for durability. The adhesive backing card and diagnostic tape seal the paper channel to prevent evaporation by Joule heating, which has been shown to cause sample dispersion effects.²³ Nitrocellulose was used as the medium for the paper channel, because it is commonly used for test strips in lateral flow assays.⁴⁰ The microbead bed, composed of super avidin microspheres, is packed directly onto the nitrocellulose and aligned such that a slight overlap exists with the cathodic Nafion membrane (Scheme 1B). Nafion was employed as the ion selective membrane necessary for ICP. Its surface contains negatively charged sulfonate (SO_3^-) groups that exclude anions from entering its pores, thus responsible for the selective transport of ions under an applied electric field.^{11,22} Fig. 1A shows a photograph of the μ b-ICP-PAD and the scale of the device. To operate the μ b-ICP-PAD, the sample solution is added to the sample pad and capillary flow is maintained with constant wicking of the solution by the absorbent pad. Voltage is applied to the Ag/AgCl driving electrodes, which are each coated with a Nafion membrane that extends across the channel's width when aligned. These Nafion-coated electrodes were previously reported in a microscale device and help mitigate faradaic reactions produced at the electrodes.⁴¹

Scheme 1B is a representation of the ICP mechanism and ion transport through the device under the presence of an electric field. Initially, there is an equal distribution of ions in the channel after being filled with buffer. The buffer (Tris-HCl) is composed of anions (red circles) and cations (blue circles). Under an applied electric field, buffer cations migrate towards the cathode and are able to enter through the pores of the cation-exchange membrane (CEM), where they are sub-





Scheme 1 Schematic overview of the paper-based ICP device used in this study. (A) Device design and a blown-up view representing BSA focusing within the packed microbead bed. (B) Mechanism of paper-based ICP as it occurs between the Nafion membranes. (C) ICPF of a negatively charged analyte whose distinct position is a function of electric field strength.

sequently consumed at the electrode. As anions are attracted to the anode and begin to migrate there, an ion depletion zone (IDZ) develops at the ion-selective membrane interface and propagates into the channel. With the arrival of anions at the anode, cations will accumulate to maintain electroneutrality, thus forming an ion enrichment zone (IEZ). At the boundary of the IDZ, a steep gradient in the electric field is present. In the presence of opposing fluid flow, analytes focus in the electric field gradient as a function of position (Scheme 1C). The analyte (red diamonds) will focus at the position in which its electrophoretic mobility and the convective forces acting on it are balanced. The convective forces in this system consist mainly of capillary flow, in the direction of the cathode. Electroosmotic flow is suppressed by the Pluronic coating of the nitrocellulose and sample pads. Scheme 1A shows a magnified view of the area between the two Nafion membranes. During ICPF, proteins will focus at the position of the microbead bed, which is overlaying the boundary of the IDZ. A sandwiched dual-gate design was employed, because it spatiotemporally confines enrichment between the two Nafion membranes for improved stability of the focused plug.^{12,37,42}

To combat the effects of electroconvection within the IDZ on sample focusing, microbeads were incorporated into the paper channel. This design was inspired by previously reported studies in which geometric restrictions have shown to improve fluidic stability during focusing. Specifically, by microstructuring the area of the IDZ, the growth of fluid vortices is phys-

ically suppressed and stable preconcentration is demonstrated.^{38,43} Fig. S1 presents SEM micrographs taken of a paper channel packed with a microbead bed to estimate the degree of embedment within the nitrocellulose fibers. On close examination of these images, there is partial penetration through the pores of the paper by the microbeads, more than 18 μm deep. Thus, the microbeads would take up part of the geometric space occupied by the IDZ during focusing. The bed also serves as a physical impediment to fluid flow along the channel. The microbead bed's impact on protein enrichment is examined in the following section.

To verify the ICP process, current-voltage curves (CVCs) were obtained between the electrodes of the μb -ICP-PAD. Fig. S2 shows the results of these measurements, with clear ohmic, limiting, and overlimiting regimes established. The power consumption of this device is 30 mW, which is 1.4-fold³² and 7-fold⁴⁴ lower than previously reported paper-based preconcentrators.

3.2. Comparison of protein enrichment in ICP-PADs with and without beads

We first investigated the impact of a packed microbead bed on the enrichment of a dye-linked protein. Texas-Red BSA was selected as the analyte, because it is an established model for demonstrating protein enrichment in ICP-PADs.¹⁰ Briefly, to conduct this experiment, Texas-Red BSA was diluted to 80 nM and 300 μL of this sample solution was applied to the sample



pad. The sample solution was then flowed for 15 min to allow for constant capillary flow to be established by the fan-shaped waste pad. Next, 70.0 V was applied ($t = 0$ min) between the two Nafion membranes for a period of 20 min. The spatial dis-

tribution of the fluorescently tagged BSA was tracked during ICPF and the resulting micrographs for the cases of no beads (Fig. 2A) and beads (Fig. 2B) are shown using a single ICP-PAD for each. The solid white lines represent the boundaries of the

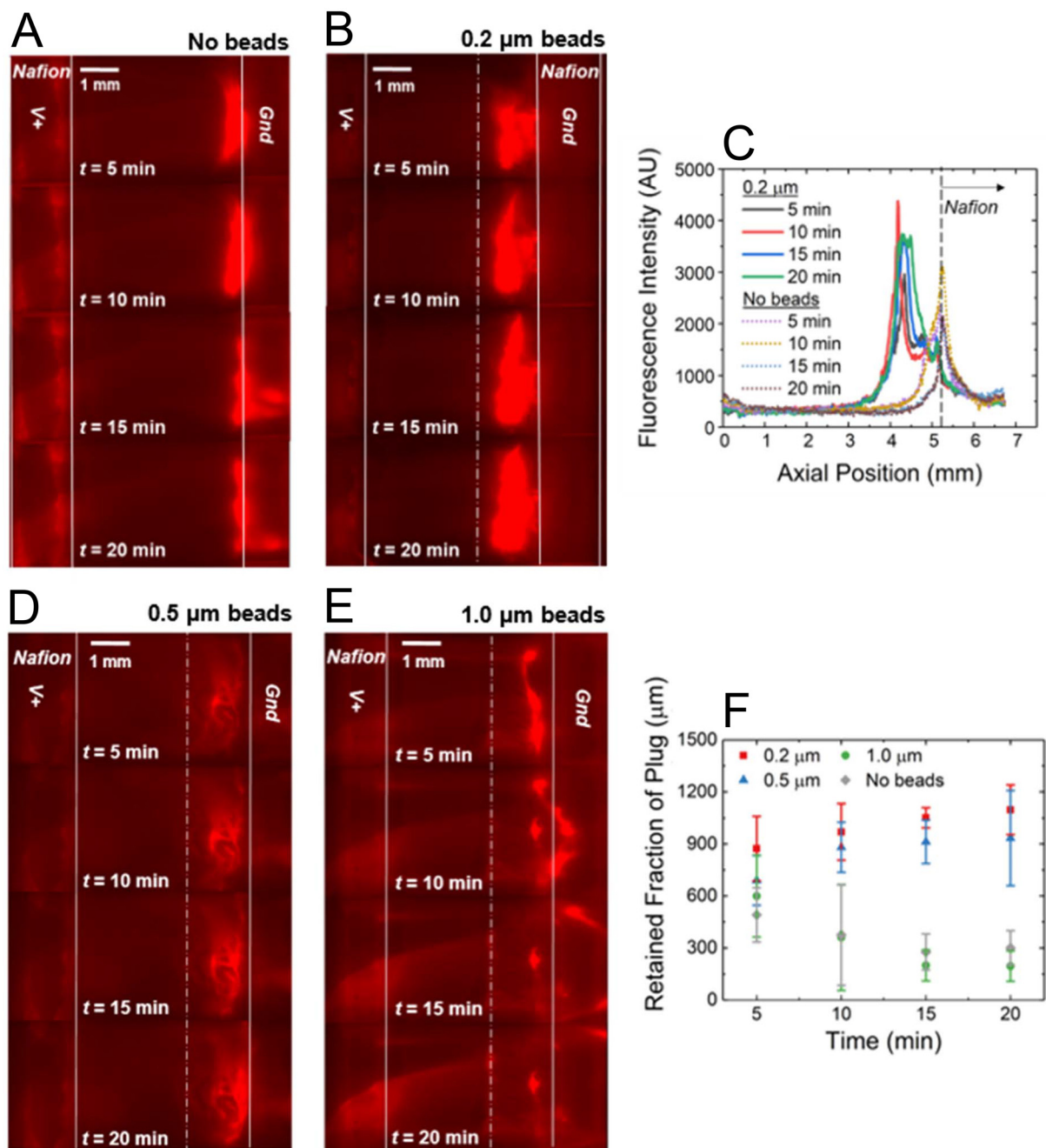


Fig. 2 Sequential fluorescence micrographs showing the position of 80 nM Texas Red BSA (100 mM Tris HCl, 0.05% Tween-20, pH 8.2) enriching within a device architecture composed of distinct microbead sizes: (A) no beads, (B) $d = 0.2 \mu\text{m}$, (D) $d = 0.5 \mu\text{m}$, and (E) $d = 1.0 \mu\text{m}$. The solid white lines represent the boundaries of the Nafion membranes, and the white dashed lines indicate the left-hand edge of the microbead bed. These sequential images were obtained after applying a voltage of 70.0 V at $t = 5, 10, 15,$ and 20 min. $V^+ = 70.0$ V at $t = 0$ min. (C) Plot of background-subtracted fluorescence intensities at distinct time points following $V^+ = 70.0$ V for the images shown in A and B. The intensities were measured along a line profile extending from the boundary of the anodic Nafion membrane and through the device. The cathodic Nafion membrane begins at 5.2 mm as indicated by the dashed black line on the plot. (F) Plot of retained fraction of the focused plug as a function of time for the four device architectures ($d = 0.2 \mu\text{m}, 0.5 \mu\text{m}, 1.0 \mu\text{m},$ and no beads). In all cases, $n = 3$.



Nafion membranes and the dashed white line indicates the beginning edge of the microbead bed. These images qualitatively reveal that a device with a packed microbead bed suppressed bursting of the protein plug for the period of enrichment. However, a device without beads showed bursting by $t = 15$ min, which is evidenced by narrowing of the focused plug and streaks of fluorescence extending downstream. It is important to note that in a device with packed beads, the shape of the focused plug is such that it covers almost the entire microbead bed and spans nearly the width of the paper by $t = 20$ min. This distribution and long-term enrichment capability are especially relevant for downstream biological assays, such as LFAs targeting low-abundance analytes.¹² Although the enrichment zone within the bead bed appears broader than that formed on bare paper, the fluorescence intensity is substantially higher (Fig. 2C). The packed microbead bed forms a porous confinement region that stabilizes the enrichment zone and prevents convective disruption of the IDZ that would otherwise lead to bursting. This is achieved without tuning experimental parameters such as voltage or flow rate.¹¹

We next evaluated the distribution of fluorescence intensity along the channel as illustrated in Fig. 2C. A line profile measuring each pixel's intensity was drawn for several time points, with each line beginning at the right-hand boundary of the anodic membrane and continuing (downstream) through the cathodic membrane. This alignment accounts for variations in how much of each Nafion membrane is visible during an experiment. Under $1\times$ magnification, approximately 8.5 mm is able to be viewed at any given time point, which includes all of the paper channel between the two membranes and all/part of the anodic/cathodic Nafion membrane. Fig. 2C shows that in the $\mu\text{b-ICP-PAD}$ Texas Red BSA focused upstream of the cathodic Nafion membrane at approximately 4.4 mm. Without a packed microbead bed, Texas Red BSA "washed over" the cathodic Nafion and focused at approximately 5.3 mm. The left-hand boundary of the cathodic Nafion membrane is noted on the graph as a dashed line occurring at the position of 5.2 mm. Low mobility analytes, such as proteins, typically "wash over" during ICPF under the experimental conditions. By employing a microbead bed, stable focusing of proteins occurs at a fixed, optimal location within the channel instead of over the Nafion membrane, thus decreasing the opportunity for membrane biofouling during an assay. A greater area under each curve is ascribed to the case of $0.2\ \mu\text{m}$ beads compared to no beads, indicating a greater amount of fluorescence intensity at respective time points and thus, greater preconcentration (Fig. 2C).

In order to quantify the degree of protein enrichment in both cases, we next determined the enrichment factors (EF). The maximum EF was measured by analyzing the background subtracted intensity of the pixels in the brightest spot (100 pixels) at each time point divided by the background subtracted initial intensity of the pixels at $t = 0$ min. The maximum EF is typically what is reported in the literature when determining the amount of preconcentration in paper-based devices.¹⁰ However, we also examined the average EF,

which was determined by averaging all of the background subtracted pixel intensities over the entire bead bed area ($>70\,000$ pixels), divided by the background subtracted initial average intensity at $t = 0$ min. The average EF is an especially relevant measurement for potential downstream applications, because it quantifies how much analyte can be enriched over a region of interest.

Fig. 3A shows that the $\mu\text{b-ICP-PAD}$ exhibited a steady increase in average EF over time of nearly 5-fold at $t = 20$ min, whereas a device without beads achieved approximately 2-fold of average enrichment by $t = 7$ min, before decreasing to near the initial state at $t = 7$ min. In terms of the maximum EF, approximately 18-fold enrichment of Texas Red BSA occurs in the presence of beads, whereas only 6-fold enrichment is seen in the case of no beads at the same time point, $t = 20$ min (Fig. 3C). In both cases (no beads and $0.2\ \mu\text{m}$ bead), the highest observed EF of 23-fold occurred with a packed microbead bed at the end of enrichment, while the peak EF for no beads was 13-fold around $t = 4$ min. Large decreases in maximum and average EF were seen for ICP-PADs without beads as the experiments progressed, because of bursting of the protein plug downstream. Additionally, we observed that once the protein analyte began to enrich in the packed microbead bed that its location was stable as it remained within the $0.2\ \mu\text{m}$ beads. A similar phenomenon was observed in a microscale device and was attributed to a higher electrical and fluidic resistance within the packed bead bed, leading to a subsequent enhancement in electric field.³⁸ Fig. S1B revealed partial penetration of the beads through the pores of the nitrocellulose, therefore taking up part of the geometric space occupied by the IDZ, and increasing the electrical resistance. As the electrical resistance increases, the electric field inside the bead bed is enhanced, which could be contributing to the higher EF in the case of beads. Greater preconcentration and EF translates to a higher sensitivity for future assay applications. Increasing average EF is especially significant for potential LFAs because the amount of antigen available increases over the entire bead bed area, resulting in greater complex formation within the assay time.¹²⁻¹⁶

3.3. Characterization of the effect of bead diameter and its impact on bursting

To determine the optimal bead diameter for stable protein enrichment in the $\mu\text{b-ICP-PAD}$, we compared three bead sizes ($d = 0.2\ \mu\text{m}$, $0.5\ \mu\text{m}$, $1.0\ \mu\text{m}$). We selected these three sizes because the porosity of the nitrocellulose membrane is rated at $0.45\ \mu\text{m}$, so that the examined microbeads are theoretically smaller/bigger/similar to the pore size of the paper channel. We carried out these experiments with the same experimental protocol as the previous subsection. The spatial distribution of protein enrichment was tracked by the fluorescence of Texas Red BSA. With $0.5\ \mu\text{m}$ beads, BSA's location remained fixed in the bead bed for the entirety of voltage application (Fig. 2D). This behavior was observed for all trials, including $0.5\ \mu\text{m}$ beads. However, BSA in the presence of $1.0\ \mu\text{m}$ beads displayed rapid enrichment at $t = 5$ min before a sudden bursting by $t =$



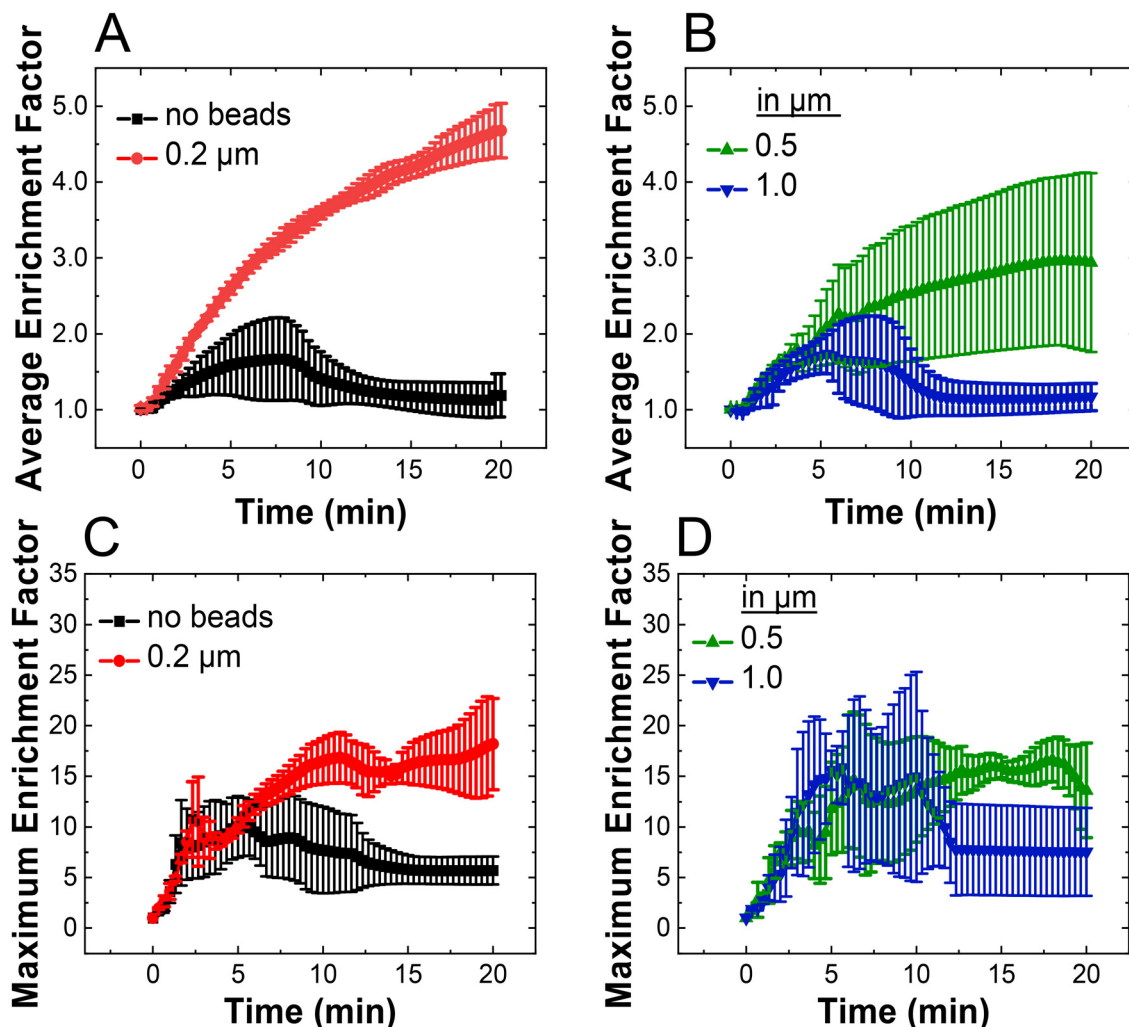


Fig. 3 Electrokinetic enrichment of 80 nM Texas Red BSA in 100 mM Tris HCl, 0.05% Tween-20, pH 8.2 ($n = 3$). $V^+ = 70.0$ V at $t = 0$ min. Plots of the average enrichment factor versus time for four device architectures: (A) unmodified nitrocellulose channel (black trace) and 0.2 μm microbead-packed bed (red trace); (B) 0.5 μm (green trace) and 1.0 μm (blue trace) microbead-packed beds. The average enrichment factor was determined by averaging all the background-subtracted intensities over a region of interest representative of the size and location of a packed microbead bed. Plots of the maximum enrichment factor versus time for the same device architectures: (C) unmodified nitrocellulose channel (black trace) and 0.2 μm microbead-packed bed (red trace); (D) 0.5 μm (green trace) and 1.0 μm (blue trace) microbead-packed beds. The maximum enrichment factor was determined by measuring the average background-subtracted intensities over the brightest spot in the focused plug. For clarity, plots (A) and (B) are shown separately to prevent overlap of standard deviation. Plots (C) and (D) are likewise presented separately for the same reason.

10 min, with only a small portion of the plug remaining by the end of the experiment (Fig. 2E). Bursting was observed for all 3 trials of 1.0 μm beads, but at differing times. Comparing all 4 cases ($d = 0.2$ μm , 0.5 μm , 1.0 μm , no beads), in respect to the width of the focused plug, we assessed the retained fraction of the protein plug at specific time points (Fig. 2F). This was obtained by measuring the widest point of the focused plug for each data set, which reflects the amount of protein retained and not lost downstream due to bursting.

Initially, the retained fraction of plug during ICPF is nearly the same in all four cases, with 0.2 μm beads having a slightly higher retention. However, by $t = 10$ min a trend emerges between devices that did or did not experience bursting, and is most pronounced at $t = 15$ and 20 min. Both 0.2 and 0.5 μm

beads suppressed bursting, or loss, of the enriched plug. Their retained fraction only increased over time, to greater than 1000 μm at $t = 20$ min. In the cases of 1.0 μm beads and no beads, loss of the focused plug occurred and only a narrow part of the band remained by the end of the experiment. At $t = 15$ min, their retained fraction decreased dramatically from approximately 600 μm to 300 μm . These results indicate $d = 0.2$ μm and 0.5 μm give rise to a greater fraction of analyte available for potential downstream analyses.

Fig. 3 shows the average and maximum EF for the three bead bed device architectures. The average EF was greatest in PADs using 0.2 μm beads (Fig. 3A). This same metric increased as a function of time for 0.5 μm beads (Fig. 3B), but decreased for 1.0 μm beads. In regards to maximum EF, 0.2 and 0.5 μm



beads have comparable EFs. However, 0.5 μm beads presented more variability in the degree of enrichment over the course of the experiment (Fig. 3D, compare with Fig. 3C). The greatest maximum EF observed for 0.5 μm beads was 21-fold at $t = 7$ min. Interestingly, 1.0 μm beads exhibited the highest initial EFs, exceeding 26-fold at $t = 10$ min, before bursting was observed (Fig. 3D). This behavior likely arises because 1.0 μm beads primarily form a surface layer on the nitrocellulose rather than penetrating into the membrane pores. In contrast, smaller beads (e.g., 0.2 μm) partially embed within the nitrocellulose fiber network and create smaller interstitial spaces, which provide stronger geometric confinement of the IDZ and help suppress electroconvective instabilities. As a result, although enrichment with 1.0 μm beads is initially strong, the resulting plug is less stable and bursts earlier than in devices containing smaller beads that penetrate more deeply into the nitrocellulose structure. The high error bars in Fig. 3D for 1.0 μm beads are representative of the variance in the time in which bursting occurred, at an interval between 3 to 10 min, following a period of rapid enrichment. We conclude from these experiments how bead diameter relates to stable and effective enrichment at a specific porosity of the paper channel.

3.4. Examination of the microbead bed and its functionality

To determine the stability of the microbead bed during the experimental procedures, dye-linked microbeads were employed in the packing of the bead bed, which enabled visualization by fluorescence. The same experimental protocol from the previous subsection was conducted, however the sample solution contained only the background electrolyte (100 mM Tris HCl, and 0.05% Tween-20). Fluorescence micro-

graphs were taken before and after ICP (Fig. 4A) where t_i indicates the start of voltage application and t_f is after 20 min at $V^+ = 70.0$ V. The white dashed lines represent the boundaries of the Nafion membranes. No discernible difference between the two time points can be seen by the naked eye. To quantitatively describe these results, the integrated intensity was measured over a region of interest drawn to encapsulate the entire packed microbead bed.

Fig. 4B shows no significant change in the integrated intensity after ICP. Less than 1% of fluorescence ($0.7 \pm 0.6\%$) produced by the microbeads was lost under the conducted experimental conditions, and these experiments were performed in three different $\mu\text{b-ICP-PADs}$. Therefore, we expect the majority of the microbead bed to be stable during electrokinetic enrichment.

3.5. Microbead bed as a test line and selectivity of the beads

Next, we designed experiments that would leverage the packed microbead bed as a test line for a model LFA (without enrichment). The polystyrene beads used in the packing of the $\mu\text{b-ICP-PAD}$ are coated with streptavidin, and therefore bind biotin with a strong affinity. To match previous experimental conditions, Texas-Red BSA was biotinylated so as to serve as the antigen in the LFA. The biotinylation of the fluorescently tagged BSA is described in detail in the SI. Briefly, a commercial labeling kit was used for the conjugation of biotin to BSA based on amine chemistry. The solution was then dialyzed overnight to ensure excess biotin was removed. Similar to the previous protocol, 300 μL of antigen was added to a device without Nafion-coated electrodes in the top and bottom layers. The fluorescence was monitored over the microbead bed and the resulting signal at the end of the assay ($t = 35$ min) was

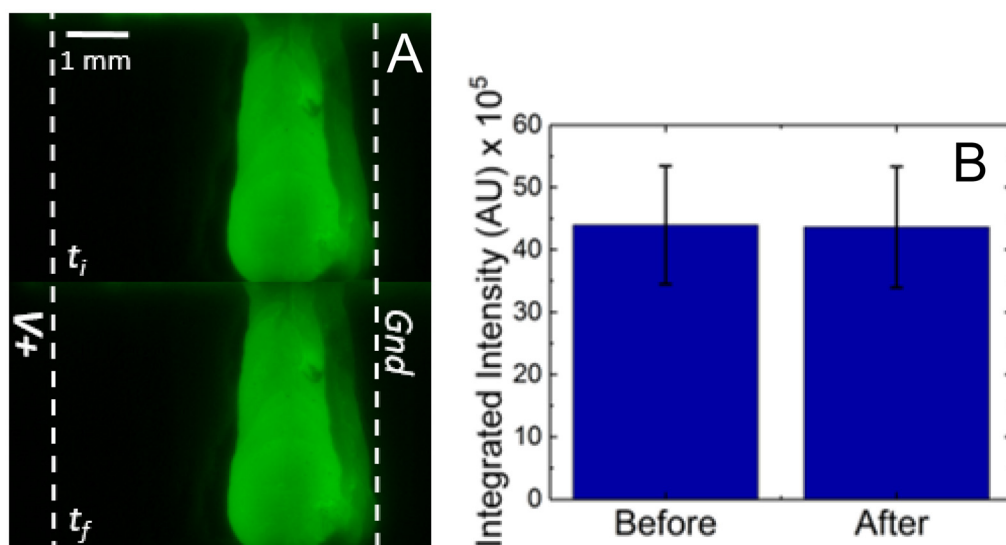


Fig. 4 Dye-linked 0.2 μm microbeads (Dragon Green) in 100 mM Tris HCl, 0.05% Tween-20, pH 8.2 (A) fluorescence micrograph of the dye-linked microbead packed in a nitrocellulose channel at t_i (before voltage application) and t_f (after 20 min of $V^+ = 70.0$ V). The white dashed lines represent the boundaries of the Nafion membranes. (B) Bar graph of the integrated intensity over the packed microbead bed before and after the ICP process, showing $0.7 \pm 0.6\%$ of fluorescence produced by the microbeads lost ($n = 3$).



recorded for a series of concentrations (10, 50, 100, 500, 1000 nM). In this LFA, the fluorescent intensity was measured after 35 min, matching the time of the previous enrichment protocol, which included 15 min of flow stabilization and 20 min of enrichment.

Fig. 5 shows the calibration curve obtained for biotinylated Texas Red BSA. Over the working concentration range of 10–1000 nM, the average fluorescence intensity increases linearly with concentration ($R^2 = 0.9912$). The limit of detection (LOD), calculated using the 3.3σ per slope criterion, was 231 nM with a sensitivity of 1.456 AU nM^{-1} .⁴⁵

Next, a negative control was performed using non-binding BSA (no biotin) in the LFA format at the concentration of 100 nM. The fluorescence signal obtained from this control represents the background level arising from nonspecific adsorption to the nitrocellulose membrane and microbead bed. Compared to biotinylated BSA, the signal was found to be significantly different at the 95% confidence level (Fig. 6). We conclude from these experiments that the packed microbead bed can function as a capturing agent for target proteins in solution.

Thus, the microbead bed serves a dual purpose: (i) stabilizing electrokinetic preconcentration by suppressing bursting, and (ii) functioning as a spatially fixed test line compatible with standard LFA architectures. Future steps would include using biotinylated capture antibodies conjugated to the microbead bed for detection of specific biomarkers. Because analytes differ in electrophoretic mobility, enrichment conditions may be adjusted for different biomarkers by modifying the applied voltage or the position of the capture region relative to the Nafion membrane.

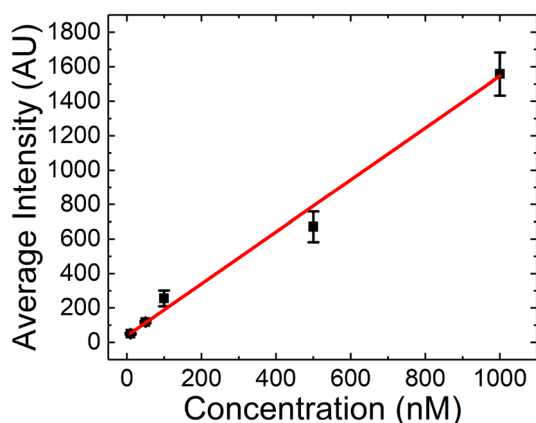


Fig. 5 Calibration curve for biotinylated BSA. Plot of background subtracted average fluorescence intensity (AU) as a function of concentration (nM) for five distinct concentrations of biotinylated Texas Red BSA (10 nM, 50 nM, 100 nM, 500 nM, 1000 nM). The signal obtained at $t = 35$ min was measured over a region of interest containing the microbead bed ($n = 3$). A linear curve fitting yielded an R^2 value of 0.9912.

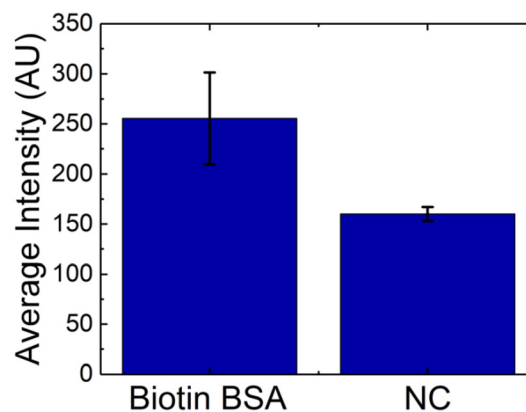


Fig. 6 Comparison of the signal for target and non-target proteins in the LFA format. Bar graph of the background subtracted average fluorescence intensity (AU) of biotinylated Texas Red BSA and a negative control, Texas Red BSA (non-binding). The signal was measured over the microbead bed at $t = 35$ min. Both protein analytes were tested at the concentration of 100 nM diluted in 100 mM Tris HCl, 0.05% Tween-20, pH 8.2. The error bars represent one standard deviation from three replicates.

Conclusions

In this paper, we addressed the core issue of the stability of the focused plug in an ICP-enhanced LFA in a paper strip and provided a simple strategy for enhanced enrichment of proteins. We demonstrated the enrichment of Texas-Red BSA within a packed microbead bed by applying ion concentration polarization in a paper-based analytical device. This μ -ICP-PAD offers several advantages with its easy fabrication and use of inexpensive materials, such as off-the-shelf microbeads patterned directly on lateral flow paper. The implications of improved protein preconcentration are a greater fraction of the target available for potential downstream assays and enhanced assay performance resulting from stable, fixed localization of the focused plug over extended periods.

This study examined the electrokinetics of proteins under several conditions to determine the impact on bursting, an undesirable phenomenon that can occur during ICPF. Monitoring of a fluorescent tracer reveals for the first time that physically adsorbed microbeads on a PAD counteract bursting, or loss, of the focused plug. Protein enrichment is greater in the case of beads than without, improving the average EF by 5-fold and the maximum EF by 4-fold, respectively. The highest observed EF of 23-fold was recorded for the μ -ICP-PAD. Under the same flow conditions, BSA enriches in the microbead bed, and not over the Nafion, as is the case with no beads, thereby avoiding the possibility of biofouling. Large amounts of bursting were attributed to devices without beads, leading to a decrease in the maximum EF to nearly 6-fold by the end of enrichment. The comparison of several bead sizes revealed that $d = 0.2$ and $0.5 \mu\text{m}$ had similar maximum EFs ($>15\times$) and retained fraction of plug ($>900 \mu\text{m}$). However, $1.0 \mu\text{m}$ beads did not deter bursting, in spite of the high



initial enrichment, and ended with a retained fraction even less than ICP-PADs without beads. Finally, we verified that the beads are stationary under the conditions of ICPF and can act as a test line for target proteins in a LFA.

Future studies in our laboratory will explore the large parametric space associated with antigens to ascertain how the μ -ICP-PAD performs as a function of the target's K_D , electrophoretic mobility, and molecular weight, as well as conductivity of the media. These studies would incorporate a LFA into the existing ICP scheme presented herein for specific applications requiring improved LODs. We anticipate this method can be easily integrated into existing paper-based assays, because it does not require modification of the lateral flow membrane chemistry or assay workflow, thereby expanding the range of analytes accessible in PADs and POC diagnostics.

Author contributions

Sommer Osman: conceptualization, methodology, formal analysis, investigation, visualization, writing – original draft. Kira L. Rahn: methodology, formal analysis, investigation. Quinlan G. Pollak: formal analysis, investigation. Md Ruhul Amin: review & editing. Robbyn K. Anand: supervision, conceptualization, writing – review & editing.

Conflicts of interest

Authors declare no competing interest.

Data availability

The data that support the findings of this study are available from the corresponding author upon reasonable request.

Supplementary information (SI): videos of Texas-Red BSA enrichment in ICP-PADs with and without beads, current-voltage curves recorded for Texas-Red BSA, experimental details for the biotinylation of Texas-Red BSAs. See DOI: <https://doi.org/10.1039/d6an00004e>.

Acknowledgements

The authors gratefully acknowledge funding through the Research Corporation for Scientific Advancement COVID Initiative (27355) and the Roy J. Carver Charitable Trust (21-5449). The authors thank Robert G. Hjort for his help in creating laser-cut stencils. In addition, Warren Straszheim and the ISU Materials Analysis and Research Laboratory are greatly appreciated for their guidance and training in SEM imaging acquisition.

References

- 1 J. C. Cunningham, P. R. Degregory and R. M. Crooks, *Annu. Rev.*, 2016, **9**, 183–202.
- 2 T. Ozer, C. McMahon and C. S. Henry, *Annu. Rev.*, 2025, **13**, 85–109.
- 3 J. Mettakoonpitak, K. Boehle, S. Nantaphol, P. Teengam, J. A. Adkins, M. Srisa-Art and C. S. Henry, *Electroanalysis*, 2016, **28**, 1420–1436.
- 4 J. E. Schonhorn, S. C. Fernandes, A. Rajaratnam, R. N. Deraney, J. P. Rollanda and C. R. Mace, *Lab Chip*, 2014, **14**, 4653–4658.
- 5 Y. Yang, E. Noviana, M. P. Nguyen, B. J. Geiss, D. S. Dandy and C. S. Henry, *Anal. Chem.*, 2017, **89**, 71–91.
- 6 X. Li, L. Luo and R. M. Crooks, *Lab Chip*, 2015, **15**, 4090–4098.
- 7 L. P. Murray and C. R. Mace, *Anal. Chim. Acta*, 2020, **1140**, 236–249.
- 8 V. Gubala, L. F. Harris, A. J. Ricco, M. X. Tan and D. E. Williams, *Anal. Chem.*, 2012, **84**, 487–515.
- 9 M. Zhiyue, Y. Xichen, R. Li, Y. Yang, F. Huicheng and S. Peng, *Electrophoresis*, 2021, **3**, 1–12.
- 10 W. Alahmad, A. Sahragard and P. Varanusupakul, *Biosens. Bioelectron.*, 2021, **194**, 113574.
- 11 B. Berzina and R. K. Anand, *Anal. Chim. Acta*, 2020, **1128**, 149–173.
- 12 K. L. Rahn, S. Y. Osman, Q. G. Pollak and R. K. Anand, *Anal. Methods*, 2023, **16**, 91–104.
- 13 M. R. Amin, B. Berzina, U. Peramune and R. K. Anand, *Analyst*, 2025, **150**, 4059–4069.
- 14 S. Osman, E. L. Claus and R. K. Anand, *Anal. Chem.*, 2023, **95**, 9337–9346.
- 15 S. U. Devasinghe, E. L. Claus, M. E. Strait, D. Pagariya and R. K. Anand, *ACS Sens.*, 2024, **9**, 5776–5781.
- 16 B. Berzina, U. Peramune, S. Kim, K. Saurabh, E. L. Claus, M. E. Strait, B. Ganapathysubramanian and R. K. Anand, *ACS Sens.*, 2023, **8**, 1173–1182.
- 17 M. Li and R. K. Anand, *Analyst*, 2016, **141**, 3496–3510.
- 18 M. M. Gong, R. Nosrati, M. C. San Gabriel, A. Zini and D. Sinton, *J. Am. Chem. Soc.*, 2015, **137**, 13913–13919.
- 19 L. H. Hung, H. L. Wang and R. J. Yang, *Microfluid. Nanofluid.*, 2016, **20**, 1–9.
- 20 S. H. Yeh, K. H. Chou and R. J. Yang, *Lab Chip*, 2016, **16**, 925–931.
- 21 N. Liu, D. T. Phan and W. S. Lew, *IEEE Trans. Biomed. Circuits Syst.*, 2017, **11**, 1392–1399.
- 22 M. M. Gong, P. Zhang, B. D. Macdonald and D. Sinton, *Anal. Chem.*, 2014, **86**, 8090–8097.
- 23 R. J. Yang, H. H. Pu and H. L. Wang, *Biomicrofluidics*, 2015, **9**, 014122.
- 24 S. I. Han, Y. K. Yoo, J. Lee, C. Kim, K. Lee, T. H. Lee, H. Kim, D. S. Yoon, K. S. Hwang, R. Kwak and J. H. Lee, *Sens. Actuators, B*, 2018, **268**, 485–493.
- 25 H. Gao, J. J. Liu, Y. Q. Liu and Z. Y. Wu, *Microfluid. Nanofluid.*, 2019, **23**, 1–7.
- 26 A. T. K. Perera, S. Pudasaini, S. S. U. Ahmed, D. T. Phan, Y. Liu and C. Yang, *Electrophoresis*, 2020, **41**, 867–874.



- 27 H. Gao, M. R. Xie, J. J. Liu, F. Fang and Z. Y. Wu, *Microfluid. Nanofluid.*, 2018, **22**, 1–8.
- 28 D. T. Phan, S. A. M. Shaegh, C. Yang and N. T. Nguyen, *Sens. Actuators, B*, 2016, **222**, 735–740.
- 29 J. Lee, Y. K. Yoo, D. Lee, C. Kim, K. H. Kim, S. Lee, S. Kwak, J. Y. Kang, H. Kim, D. S. Yoon, D. Hur and J. H. Lee, *Lab Chip*, 2021, **21**, 867–874.
- 30 K. Lee, Y. K. Yoo, S. I. Han, J. Lee, D. Lee, C. Kim and J. H. Lee, *Micro Nano Syst. Lett.*, 2017, **5**, 1–7.
- 31 K. H. Chou, S. H. Yeh and R. J. Yang, *Microfluid. Nanofluid.*, 2017, **21**, 1–12.
- 32 S. I. Han, K. S. Hwang, R. Kwak and J. H. Lee, *Lab Chip*, 2016, **16**, 2219–2227.
- 33 X. Li, L. Luo and R. M. Crooks, *Anal. Chem.*, 2017, **89**, 4294–4300.
- 34 R. A. Ruiz, J. L. Gonzalez, M. Vazquez-Alvarado, N. W. Martinez and A. W. Martinez, *Anal. Chem.*, 2022, **94**, 8833–8837.
- 35 A. Espinosa, J. Diaz, E. Vazquez, L. Acosta, A. Santiago and L. Cunci, *Talanta Open*, 2022, **6**, 100142.
- 36 S. H. Ko, Y. A. Song, S. J. Kim, M. Kim, J. Han and K. H. Kang, *Lab Chip*, 2012, **12**, 4472–4482.
- 37 R. Kwak, J. Y. Kang and T. S. Kim, *Anal. Chem.*, 2016, **88**, 988–996.
- 38 B. Berzina, S. Kim, U. Peramune, K. Saurabh, B. Ganapathysubramanian and R. K. Anand, *Lab Chip*, 2022, **22**, 573–583.
- 39 J. A. Adkins, E. Noviana and C. S. Henry, *Anal. Chem.*, 2016, **88**, 10639–10647.
- 40 C. A. Holstein, A. Chevalier, S. Bennett, C. E. Anderson, K. Keniston, C. Olsen, B. Li, B. Bales, D. R. Moore, E. Fu, D. Baker and P. Yager, *Anal. Bioanal. Chem.*, 2016, **408**, 1335–1346.
- 41 R. Kwak and J. Han, *J. Phys. Chem. Lett.*, 2018, **9**, 2991–2999.
- 42 C. Kim, Y. K. Yoo, S. Il Han, J. Lee, D. Lee, K. Lee, K. S. Hwang, K. H. Lee, S. Chung and J. H. Lee, *Lab Chip*, 2017, **17**, 2451–2458.
- 43 K. Kim, W. Kim, H. Lee and S. J. Kim, *Nanoscale*, 2017, **9**, 3466–3475.
- 44 B. Y. Moghadam, K. T. Connelly and J. D. Posner, *Anal. Chem.*, 2014, **86**, 5829–5837.
- 45 ICH Q2, Validation of Analytical Procedures: Test and Methodology, November 2005.

